# Manipulating magnetism in $La_{0.7}Sr_{0.3}MnO_3$ via piezostrain

J. Heidler,[1,2] C. Piamonteze,[1,*] R. V. Chopdekar,[1,3,4] M. A. Uribe-Laverde,[5] A. Alberca,[1,5] M. Buzzi,[1] A. Uldry,[6] B. Delley,[6] C. Bernhard,[5] and F. Nolting[1]

[1]*Swiss Light Source, Paul Scherrer Institut, 5232 Villigen PSI, Switzerland*
[2]*SwissFEL, Paul Scherrer Institut, 5232 Villigen PSI, Switzerland*
[3]*Laboratory for Micro- and Nanotechnology, Paul Scherrer Institut, 5232 Villigen, Switzerland*
[4]*Department of Chemical Engineering and Materials Science, University of California-Davis, Davis, California 95616, USA*
[5]*University of Fribourg, Department of Physics, Fribourg Centre for Nanomaterials, 1700 Fribourg, Switzerland*
[6]*Condensed Matter Theory Group, Paul Scherrer Institut, 5232 Villigen PSI, Switzerland*

We present a detailed study of the ferromagnetic/ferroelectric heterostructure $La_{0.7}Sr_{0.3}MnO_3$/[Pb$(Mg_{1/3}Nb_{2/3})O_3]_{0.68}$-[$PbTiO_3]_{0.32}$ (011), where reversible electrical switching induces a 10 K shift of the magnetic Curie temperature $T_C$. Two distinct polarization configurations can be set in the ferroelectric substrate and are stable at remanence; reciprocal space maps highlight the accompanying lattice parameter changes which impose a biaxial strain on the manganite thin film. The magnetic response to the strain changes is probed by temperature dependent Mn $L_{3,2}$ x-ray magnetic circular dichroism and resistance measurements. X-ray natural linear dichroism spectra for both strain states probe the valence charge anisotropy: The existing population imbalance between out-of-plane and in-plane oriented orbitals increases further with tensile strain, favoring orbital occupation in the surface plane. Multiplet and density functional theory calculations support the emerging picture that an increase in tensile in-plane strain leads to an increased energy difference between the two $e_g$ orbitals and a larger Mn-O-bond length. Increasing the electron-lattice coupling and reducing the $e_g$ electron itinerancy that leads to ferromagnetism due to double exchange coupling, results ultimately in lower $T_C$ values.



## I. INTRODUCTION

Artificial multiferroics such as ferromagnetic (FM)-ferroelectric (FE) heterostructures are a route to obtain strong magnetoelectric (ME) coupling at room temperature [1]. The interactions between the magnetic and electric order parameters are not only of scientific but also of technological interest, as they could allow electric control of magnetic properties and lead to new device concepts, e.g., multiferroic tunnel junctions [2]. Several mechanisms can cause magnetoelectric coupling. In composites of piezoelectric (ferroelectric) and magnetostrictive (ferromagnetic) compounds an applied electric field induces lattice deformation in the piezoelectric constituent which is mechanically transferred to the magnetostrictive layer leading to a change in magnetization [3]. In addition to strain the magnetoelectric coupling may be ascribed to interface mechanisms such as charge screening: Ferromagnetic electrodes have to screen the polarity of adjacent ferroelectric layers leading to an accumulation of spin-polarized carriers [4–6].

An interesting class of materials are complex perovskite oxides like the doped manganites ($RE_{1-x}A_xMnO_3$, RE = rare earth, A = alkaline metal) since they display a strong interplay between electron transport, magnetism, and crystal lattice distortions making them very susceptible to charge- and strain-related changes. In these compounds a manganese ion is surrounded by an oxygen octahedron. The doping concentration defines the distribution of $Mn^{3+}/Mn^{4+}$ leading to a rich phase diagram [7]. Interfacial charge can affect this distribution and strain can cause rotations of $MnO_6$ octahedra as well as changes in the Mn-O bond lengths. Strain also has an impact on the orbital occupation. For $Mn^{3+}$ in a cubic crystal field the 3d states are split into three degenerate $t_{2g}$ and two degenerate $e_g$ levels. The resulting electronic ground state is a high spin state, where each of the $t_{2g}$ orbitals and one of the $e_g$ orbitals is singly occupied. The degeneracy of the $e_g$ orbital occupation is lifted by the Jahn-Teller effect, leading to a $MnO_6$ octahedra distortion [8].

Epitaxial strain has a similar effect favoring one direction of octahedral distortions by lowering the symmetry of the crystal field. The physics of the doped manganites is governed by the competition between the localizing effect of a strong electron-lattice coupling and the Mn $e_g$ electron itinerancy leading to ferromagnetism due to double exchange coupling [9]. Millis *et al.* introduced a model that links the dependence of the Curie temperature $T_C$ in ferromagnetic manganite films to hydrostatic and biaxial strain. Hydrostatic compression (expansion) will increase (decrease) the electron hopping amplitude and thereby reduce (increase) the electron-lattice coupling resulting in higher (lower) $T_C$ values [9]. Volume preserving biaxial or shear strain increases the energy difference between the $e_g$ levels imposed by Jahn-Teller distortion, reinforcing the electron tendency to be localized, thus determining a reduction of the Curie temperature.

Considerable work has explored the strain dependence of manganite thin films [10–15]. The magnetic properties of manganites in bulk [10] and thin films [11] have been found to be very susceptible to hydrostatic pressure. Also, the substitution of rare-earth cations with different radii acts as a source of chemical pressure, such that larger cation

*Author to whom correspondence should be addressed: cinthia.piamonteze@psi.ch

sizes correspond to higher Curie temperatures [16–19]. Tsui *et al.* have studied the effects of strain on the anisotropy and Curie temperature of $La_{0.7}Sr_{0.3}MnO_3$ (LSMO) using various substrates resulting in strained films [12]. Strain-induced anisotropy is typically dominating over the weak magnetocrystalline anisotropy in LSMO [12,20,21]. Strain dependent orbital occupation for LSMO (001) grown on different substrates has been investigated employing x-ray linear dichroism [13,22,23]: Tensile (compressive) in-plane strain favors the occupation of orbitals laying in the surface plane (pointing out-of-plane). Besides employing structural mismatch during growth the tunability of anisotropy and Curie temperature via electric fields has been the subject of many studies. Thiele *et al.* reported on piezoelectrically induced biaxial compression in a heterostructure consisting of a thin film of LSMO grown on the relaxor ferroelectric $[Pb(Mg_{1/3}Nb_{2/3})O_3]_{(1-x)}$-$[PbTiO_3]_x$ (PMN-PT) (001) [21]. Changes in $T_C$ as well as in magnetization were detected in an applied electric field, but vanished at remanence. Yang *et al.* observed an in-plane rotation of the magnetic easy axis in LSMO/PMN-PT($x = 0.3$) (011) due to an electric field [24]. The induced rotation did not remain once the bias field was switched off.

Our approach is based on the request for electrically switchable changes in LSMO thin film magnetization that are stable at remanence. We investigate the magnetoelectric coupling in a bilayer LSMO/PMN-PT ($x = 0.32$) (011) studying the magnetic response of LSMO to a ferroelectric substrate that can exhibit two distinct remanent strain states in the (011) cut. We find reversible electrical switching resulting in a 10 K shift of the $T_C$ value. X-ray diffraction (XRD) reciprocal space maps give a complete picture of the PMN-PT lattice deformations, which induce the magnetization change in LSMO. Changes in crystal field during the switching process are highlighted in x-ray natural linear dichroism (XNLD) measurements and multiplet calculations. Density functional theory (DFT) calculations give details on the electron re-distribution between $e_g$ orbitals. The paper is organized as follows: Section II gives a brief summary on the experimental details and calculations. Section III A presents results on a strain induced modulation of the magnetic anisotropy and a change in Curie temperature employing x-ray magnetic circular dichroism (XMCD). The anisotropic in-plane strain that triggers the magnetization changes is explored in Sec. III B using XRD reciprocal space maps. Section III C presents XNLD measurements and explains the change in crystal field with a population shift within the orbital $e_g$ occupation linking the former XRD results with multiplet calculations. The discussion in Sec. IV provides the link between the former result sections.

## II. METHODS

### A. Sample fabrication and experimental details

$[Pb(Mg_{1/3}Nb_{2/3})O_3]_{(1-x)}$-$[PbTiO_3]_x$ is a relaxor ferroelectric (FE) crystallizing in the perovskite $ABO_3$ structure, where the A site is occupied by a $Pb^{2+}$ ion, while the B site is randomly occupied by $Mg^{2+}$, $Nb^{5+}$, and $Ti^{4+}$ ions [25]. It shows a high piezoelectric response close to the morphotrophic

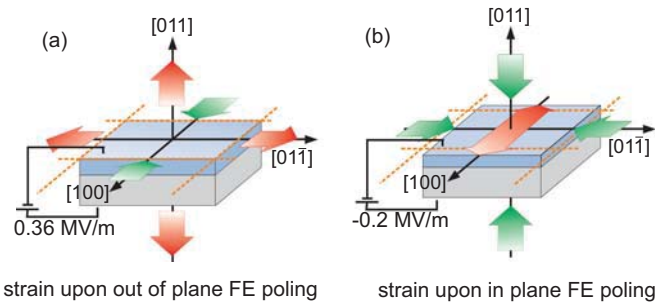


FIG. 1. (Color online) Schematic of the two distinct strain states in LSMO/PMN-PT that can be set by an electric field. (a) Strain state for OOP poled FE polarization. (b) At the coercive electric field the majority of the domains have FE polarization lying in the plane of the sample. The polarization rotation is accompanied by a large change of both IP and OOP strain imposed on the LSMO thin film, red (green) arrows represent tensile (compressive) strain, respectively.

phase boundary ranging from $x = 0.31$ to $x = 0.37$ [26]. For $x = 0.32$ doping the crystal structure is monoclinic with lattice constants $a = 4.02$ Å, $b = 4.01$ Å, and $c = 4.03$ Å [26]. Wu and coworkers reported on two reversible and remanent strain states for PMN-PT with $x = 0.32$ (011)pc (pc for pseudocubic; in the following this index will be omitted) [27]. Figure 1 shows the two distinct strain states that can be set by an applied voltage. Above the coercive field FE domains align in parallel sharing an out-of-plane (OOP) lattice constant of $c = 4.03$ Å. In the following we refer to those domains as being in an OOP poled state. Reversing the applied voltage, the FE polarization aligns parallel to the surface plane, once the coercive field is reached. We will refer to this configuration as the in-plane (IP) poled state. Note that these states are also stable at remanence. Accompanying lattice parameter changes are discussed in Sec. III B. The (011) PMN-PT single crystal ferroelectrics used in this paper were manufactured by Atom Optics Co., LTD. (Shanghai, China) using the modified Bridgman growth method with a nominal percentage of 32% $TiO_2$ powder. An 8 nm thick film of LSMO has been grown on PMN-PT ($x = 0.32$) (011) by pulsed laser deposition. The film was synthesized from a stoichiometric target using a laser fluence of 1.3 $J/cm^2$ at a repetition rate of 0.5 Hz while the PMN-PT substrate was kept at a constant temperature of 660 °C in a 300 mTorr $O_2$ ambient environment. With a pseudocubic bulk lattice constant of 3.878 Å LSMO grows in tension on PMN-PT, with detailed characterization given in Sec. III B.

XMCD and XNLD [28] measurements at the Mn $L_{3,2}$ edges were carried out at the X-Treme beamline [29] at the Swiss Light Source, Paul Scherrer Institut, Switzerland. In XMCD the intensity difference between left circular polarized ($c_+$) and right circular ($c_-$) polarized light is an element sensitive probe of the magnetization along the photon propagation direction. Sum rules allow for the determination of quantitative values for the Mn orbital and spin moment from analysis of the XMCD spectra [30,31]. X-ray absorption spectra (XAS) taken with linearly polarized light contain information on the orbital occupation of the Mn 3d orbitals along the x-ray polarization direction. The XNLD calculated as the intensity difference between the spectra measured with linear horizontal

(LH) and linear vertical (LV) polarized light arises due to an anisotropy of the valence charge distribution along respective directions. Here, in normal incidence the $(01\bar{1})$ and (100) directions are probed. From all XAS spectra a constant background was subtracted at the pre-edge. XMCD difference spectra $(c_+ - c_-)$ and XNLD difference spectra (LH-LV) were normalized to the $L_3$ XAS peak height. Measurements were done in total electron yield mode. The FE polarization of the substrate was switched in situ applying the respective electric field values. Temperature dependent XAS measurements for both poling states were done at remanence on substrates originally poled at 250 K. The superconducting magnet has a remanent field [29] ranging from 40 to 100 Oe.

The XRD was performed with a four-circle diffractometer Rigaku SmartLab (Cu K $\alpha$ radiation). The OOP lattice parameters were obtained from symmetric $2\theta - \omega$ scans. The IP lattice parameters were derived from reciprocal space maps (RSM) around the $(\bar{2}22)$ and (031) Bragg peaks of the PMN-PT substrate.

### B. Multiplet calculations

The influence of biaxial in-plane strain on XAS spectra is investigated using multiX [32] multiplet calculations (see Sec. III C). The code multiX facilitates the study of spectroscopic effects arising from low symmetry environments. The ground state and core hole state giving rise to the multiplet structure are determined under consideration of a crystal field, which is constructed explicitly from the positions of neighboring point charges interacting with the open shells of the considered Mn atom. For ferromagnetic LSMO $x = 0.33$, the crystal field is introduced by an $xyz$-coordinate file containing the positions and charges of surrounding La (Sr), Mn, and O atoms in rhombohedral symmetry [33]. As the elements La and Sr inhabit nominally the same positions in the crystal lattice, $LaMnO_3$ and $SrMnO_3$ coordinate files are treated separately in the calculations, and the resulting XNLD spectra are weighted according to the doping concentration of LSMO $x = 0.33$. XNLD spectra are calculated for $LaMnO_3$ with a $Mn^{3+}$ configuration (ground state $2p^6\ 3d^4$), as well as for $SrMnO_3$ with a $Mn^{4+}$ configuration (ground state $2p^6\ 3d^3$). In analogy to the normal incidence geometry of the experiment, $(01\bar{1})$ and (100) were chosen as linear polarization directions of the incoming light. A crystal field scaling factor of 1.7 was used to correct for the point-charge approximation. The Coulomb interaction parameter was set to 0.8. The $2p$ spin-orbit coupling defines the separation between the $L_3$ and $L_2$ edges, and the atomic value was used. The $3d$ spin orbit coupling was set to zero justified by the negligible orbital moment obtained from sum rules analysis, see Sec. III A. A Boltzmann distributed population of the initial states reflects the experimental temperature setting of about 300 K. A core-hole lifetime broadening of 0.3 was set for the $L_3$ edge; it was linearly increased from 0.3 to 0.4 over the $L_2$ edge.

## III. RESULTS

### A. XMCD and XAS measurements

Figure 2 compares Mn $L_{3,2}$ XMCD measurements for the two distinct strain states of LSMO/PMN-PT (011) at 250 K,

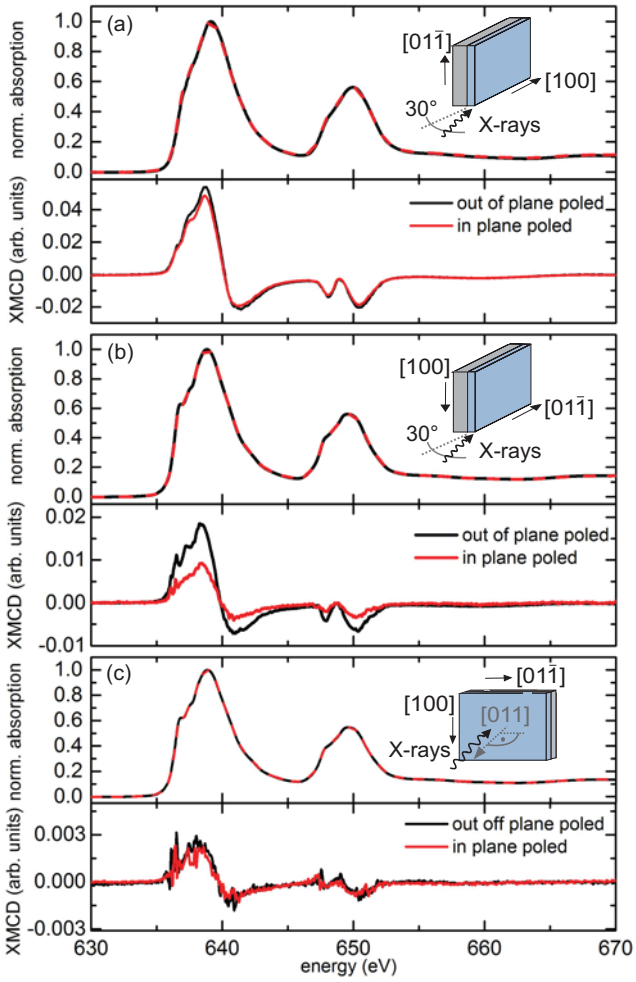


FIG. 2. (Color online) Mn $L_{3,2}$ polarization averaged XAS (top) and XMCD difference spectrum (bottom) measured in remanence at 250 K along different crystallographic directions: (a) projection along (100), (b) projection along $(01\bar{1})$, (c) projection along (011). Black (red) curves correspond to OOP (IP) poled PMN-PT substrate.

which is below the ferromagnetic Curie temperature. Black (red) curves were measured for OOP (IP) poled PMN-PT at 0 T after saturating at 3 T. Insets depict the geometry that allows for the measurement of the respective magnetization projection along (100), $(01\bar{1})$, and (011). Figure 2(a) reports the XAS spectrum (upper curve) and XMCD difference spectrum (lower curve) measured along the (100) direction in 30° grazing incidence. Comparing measurements for OOP and IP poled substrate, the XAS does not change, but the XMCD is reduced in the IP poled state. This change in magnetization upon switching is most pronounced for the spectra measured along the $(01\bar{1})$ direction, see Fig. 2(b). The difference at the $L_3$ edge measured for the OOP poled substrate reduces to half its value once the substrate is electrically switched to the IP state. Normalized XAS and XMCD measurements along the (011) direction are shown in Fig. 2(c). The effective Mn spin magnetic moment $m_{s,\mathrm{eff}}$ and orbital magnetic moment $m_{\mathrm{orb}}$ along the different crystallographic directions is extracted from the spectra in Fig. 2 using sum rules [30,31]. An example of the analysis is given in Fig. 3(a) for the XAS spectrum (after

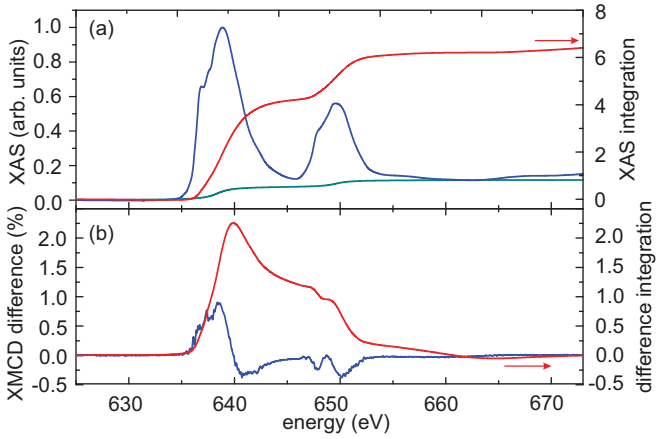


FIG. 3. (Color online) Example of the sum rules analysis for the XAS (a) and XMCD (b). Red lines show the integrated area of each spectrum (blue). The XAS was corrected by the subtraction of a baseline (green).

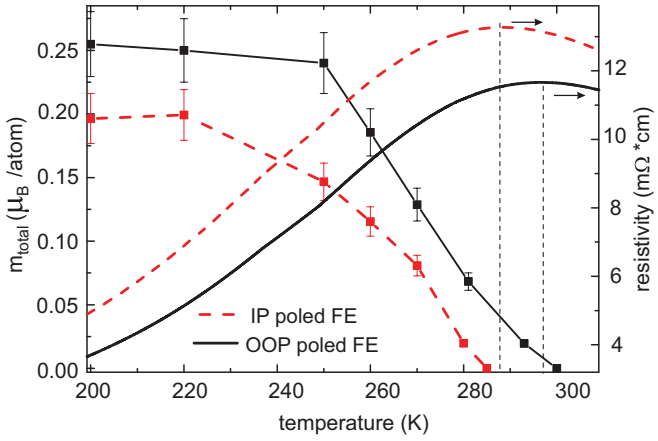


FIG. 4. (Color online) Magnetic moment along the $(01\bar{1})$ axis at remanence and resistivity as a function of temperature. Red dashed lines correspond to IP poled FE, black lines correspond to OOP poled FE.



subtraction of a background) and Fig. 3(b) for the XMCD difference spectrum, respectively.

Here, a number of 4.3 electrons per Mn ion was assumed [34,35]. Multiplet calculations using Cowan's Code [36] yield a spin correction factor of 1.52, to disentangle the overlap of the $L_3$ and $L_2$ parts in the spectrum. Table I lists $m_{s,\mathrm{eff}}$ and $m_{\mathrm{orb}}$ for both strain states. The orientation of $m_{s,\mathrm{eff}}$ and $m_{\mathrm{orb}}$ is antiparallel, consistent with the third Hund's rule in the case of a less than half-filled $d$ shell.

The total magnetic moment $m_{\mathrm{tot}} = m_{s,\mathrm{eff}} + m_{\mathrm{orb}}$ is dominated by the spin magnetic moment. The orbital moment is mostly quenched by the crystal field as expected. Table I confirms the OOP direction (011) as the hard axis, and the magnetization is pointing parallel to the surface as expected for LSMO thin films. As for the in-plane directions, (100) is the easy axis and $(01\bar{1})$ the hard axis. Both in-plane directions yield a smaller projected $m_{\mathrm{tot}}$ once the substrate is in the IP poled state. Though the IP switching may be accompanied by an anisotropy change, it is not the only effect at play: If the observed changes upon switching would be a mere rotation of the anisotropy, a decrease in $m_{\mathrm{tot}}$ along one in-plane axis would be accompanied by an increase along the perpendicular in-plane direction. Table I also gives values of the spin and orbital magnetic moments along the $(01\bar{1})$ direction taken at a magnetic field of 4 T. At saturation, the poling direction does not influence the total magnetic moment within the experimental error, yielding $m_{\mathrm{tot}} = 1.70 \pm 0.17\ \mu_B$/Mn and $m_{\mathrm{tot}} = 1.71 \pm 0.18\ \mu_B$/Mn for OOP poling and IP poling at 250 K. The saturated Mn total moment $m_{\mathrm{tot}} = 3.36 \pm 0.34\ \mu_B$/Mn measured at 50 K is comparable to the typical low temperature value for bulk LSMO $\sim 3.6\ \mu_B$/Mn [15].

XMCD measurements as a function of temperature are used to determine $T_C$ of the LSMO film. Figure 4 shows the temperature dependence of $m_{\mathrm{tot}}$ along the $(01\bar{1})$ axis at remanence. For the OOP poled substrate the magnetic moment vanishes at 300 K (black curve). Switching the FE polarization of the PMN-PT to the IP poled state, $T_C$ shifts by $-10$ K (red curve). The electrical switching thus results in different Curie temperatures. XMCD probes a particular direction of the magnetization. Resistance measurements as a function of temperature for both poling states, also shown in Fig. 4, exclude a mere rotation of the moments away from the $(01\bar{1})$ direction. The correlation between resistivity and $T_C$ can be understood from the double exchange mechanism where a FM spin alignment of neighboring Mn sites favors conductivity [37], hence resistivity measurements are widely used to determine the onset and evolution of ferromagnetism in manganite films [8,38]. Here, the resistivity measurements yield approximate $T_C$ values of 298 K (288 K) for OOP (IP) poled PMN-PT indicated by the maxima in the resistivity curves. The resistance measurements confirm the $T_C$ shift of the XMCD measurements. The measured $T_C$ values are somewhat reduced compared to the bulk value of about 370 K [39,40], as expected for thin films [12,41].

TABLE I. Projected effective Mn spin moment $m_{s,\mathrm{eff}}$ and orbital moment $m_{\mathrm{orb}}$ along different crystallographic directions for both OOP and IP poled FE substrate at 250 K extracted from Fig. 2.

| Crystallographic | OOP poled polarization | | IP poled polarization | |
|---|---|---|---|---|
| direction | $m_{s,\mathrm{eff}}$ ($\mu_B$/Mn) | $m_{\mathrm{orb}}$ ($\mu_B$/Mn) | $m_{s,\mathrm{eff}}$ ($\mu_B$/Mn) | $m_{\mathrm{orb}}$ ($\mu_B$/Mn) |
| along (100) | $0.84 \pm 0.08$ | $-0.024 \pm 0.005$ | $0.73 \pm 0.07$ | $-0.024 \pm 0.005$ |
| along $(01\bar{1})$ | $0.24 \pm 0.02$ | $-0.0007 \pm 0.0001$ | $0.15 \pm 0.01$ | $-0.0026 \pm 0.0005$ |
| along (011) | $0.026 \pm 0.003$ | $-0.0013 \pm 0.0003$ | $0.026 \pm 0.003$ | $-0.0013 \pm 0.0003$ |
| along $(01\bar{1})$ at 4 T | $1.72 \pm 0.17$ | $-0.019 \pm 0.004$ | $1.75 \pm 0.17$ | $-0.039 \pm 0.008$ |

The heterostructure allows for reversible electrical switching of the Curie temperature. The anisotropic in-plane strain triggering the $T_C$ change is explored in detail in the following section.

### B. X-ray diffraction—2D space maps

For PMN-PT (011), several voltage-dependent biaxial strain gauge measurements are reported [24,27]. However, they can only provide strain values along two respective in-plane directions. Furthermore, when using strain gauges the piezoelectric substrate is glued to the sensor via a relatively thick layer of glue which can lead to an underestimation of the absolute strain value. XRD circumvents those problems measuring the lattice parameters of the crystal in all three dimensions *in situ*.

The crystal structure of both FE IP and OOP poled PMN-PT was determined performing XRD mappings around symmetrical and asymmetrical diffraction peaks. Measurements were done at remanence after electrical switching at 300 K, therefore the coercive field is slightly smaller than the one observed in the XMCD measurements taken at 250 K. Figure 5 shows reciprocal space maps (RSM) for (011), (031), and $(\bar{2}22)$ reflections on LSMO/PMN-PT (011). Starting with a positively OOP poled PMN-PT substrate, Fig. 5(a) shows a single (011) reflection with $q_{[011]} = 0.3508$ Å$^{-1}$ corresponding to a lattice constant $c \sim \sqrt{2}/q_{[011]} = 4.031$ Å. Reversing the applied voltage the FE polarization rotates in-plane at the coercive electric field of $-0.14$ MV/m. In the (011) RSM in Fig. 5(b) a second reflection evolves at $q_{[011]} = 0.3532$ Å$^{-1}$ due to the IP poled domains. Not all domains have switched, as can be seen in Fig. 5(b), since both reflections coexist with an intensity ratio of ~60/40 for IP/OOP domains. As a larger $q_{[011]}$ value implies a smaller interplanar spacing, the electrical switching of the FE polarization from OOP to IP induces a contraction of $-0.68\%$. The RSM of the (031) reflection in Fig. 5(c) confirms the values of $q_{[011]}$ for OOP and IP poled domains in Fig. 5(b), since the measured $q_{[022]}$ values are just multiples of the $q_{[011]}$ values. In addition, the (031) RSM allows us to deduce the voltage induced strain along $(01\bar{1})$: Switching the FE polarization of the substrate to IP leads to a contraction of $-0.23\%$ along $(01\bar{1})$. Finally, the $(\bar{2}22)$ RSM in Fig. 5(d) shows that IP poling results in a change of tensile strain of $+0.90\%$ along the (100) direction. All $q$ values are listed in Table II. The RSMs give the complete picture of the resulting lattice changes in PMN-PT upon switching. Besides the induced strain change upon switching, it is important to know the epitaxial strained state of the LSMO thin film compared to bulk. Figure 5(e) and 5(f) show a larger section of the (031) and $(\bar{2}22)$ RSMs that allow us to give estimates for the LSMO lattice growth. The reflection corresponding to the LSMO thin film is seen in Figs. 5(e) and 5(f) in the upper right corner with respect to the PMN-PT reflection. The small finite number of diffracting planes in the case of a thin film leads to a spreading of the reflection peak in reciprocal space. However, it can be seen that only a partial lattice relaxation occurs. The expected peak positions for a fully relaxed film are indicated by an asterisk. The (031) RSM in Fig. 5(e) shows the OOP poled state. Having its maximum at $q_{[01\bar{1}]} = 0.3558$ Å$^{-1}$,

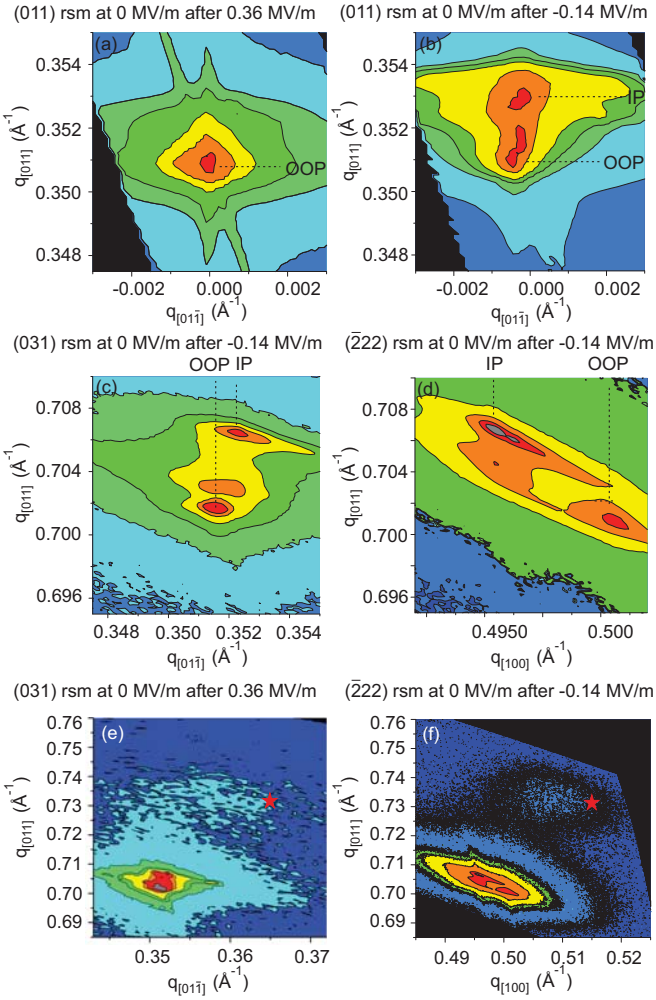


FIG. 5. (Color online) Reciprocal space maps for (011), (031), and $(\bar{2}22)$ reflections on PMN-PT (011) for both strain states. (a) For OOP poled PMN-PT the (011) RSM shows a single reflection. (b) For the IP poled state the (011) RSM shows an additional reflection corresponding to IP poled domains. When switching the FE polarization from OOP to IP, the (031) RSM in (c) highlights an IP contraction along $(01\bar{1})$, and the $(\bar{2}22)$ RSM in (d) shows a respective tensile strain change along (100). (e) and (f) show reflections of both substrate and the LSMO thin film, and asterisks mark the expected peak positions for a fully relaxed LSMO film.

LSMO grows with approximately $+2.49 \pm 0.14\%$ tensile strain along the $(01\bar{1})$ direction with respect to its bulk value. Regarding the OOP direction (011), LSMO grows compressed by about $-0.40 \pm 0.05\%$. Figure 5(f) shows a $(\bar{2}22)$ RSM for the IP poled state. Within the broad reflection peak, the two maxima corresponding to IP and OOP poled domains cannot be resolved separately. The broad maximum at $q_{[100]} = 0.5080$ Å$^{-1}$ corresponds to an average of $+1.52 \pm 0.02\%$ tensile strain along the (100) direction. Therefore the strain of the LSMO film differs along perpendicular in-plane directions.

### C. Strain dependent x-ray natural linear dichroism

XNLD at the Mn $L_{3,2}$ edges is employed to probe the anisotropy of the Mn 3*d* orbital occupation in LSMO/PMN-

TABLE II. $q$ values extracted from the RSMs for OOP and IP poled PMN-PT domains and resulting relative lattice parameter change along different crystallographic directions. Errors in $q$ are smaller than $\pm 1.44$ e-5 Å$^{-1}$ and $\pm 1.25$ e-5 Å$^{-1}$ for IP and OOP domains, respectively.

| | | OOP poled FE | IP poled FE | lattice change switching from OOP to IP |
|---|---|---|---|---|
| RSM (011) | $q_{[011]}$ in (Å$^{-1}$) | 0.3508 | 0.3532 | −0.68% |
| RSM (031) | $q_{[022]}$ in (Å$^{-1}$) | 0.7015 | 0.7064 | −0.71% |
| | $q_{[01\bar{1}]}$ in (Å$^{-1}$) | 0.3515 | 0.3523 | −0.23% |
| RSM ($\bar{2}22$) | $q_{[022]}$ in (Å$^{-1}$) | 0.7016 | 0.7066 | −0.72% |
| | $q_{[100]}$ in (Å$^{-1}$) | 0.5007 | 0.4962 | +0.90% |

PT (011) upon electric switching. Measured above $T_C$ and with no magnetic field applied, the observed difference has no magnetic linear dichroism contribution and thus represents a change in crystal field. The results are reported in Fig. 6.

In normal incidence, vertically polarized light probes the (100) direction, horizontally polarized light probes the (01$\bar{1}$) [for the measurement geometry, see the inset in Fig. 6(a)]. The x-ray polarization averaged XAS both for OOP (black) and IP (red) poled PMN-PT are shown in Fig. 6(a). Comparing the two distinct strain states the XAS does not change. Figure 6(b) depicts the XNLD for the OOP poled (black) and the IP poled (red) state. Upon electrical switching the shape of the XNLD spectra is similar, but the relative XNLD signal intensity almost doubles for the IP poled state. Being above $T_C$, the observed difference reflects a change in crystal field. Atomic multiplet calculations help to clarify in which way changes in crystal field affect XAS spectra. In Figs. 6(c) and 6(d) we compare the experimental XNLD to multiX multiplet calculations. Starting with a coordinate file of rhombohedral symmetry for LSMO

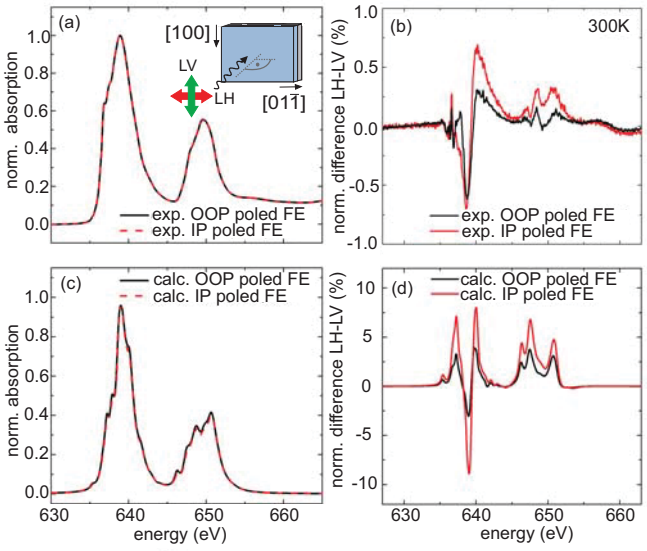


FIG. 6. (Color online) Mn $L_{3,2}$ normalized polarization averaged XAS from experiment (a) and multiplet calculations (c) for out of plane poled (black) and in-plane poled (red) PMN-PT at 300 K. The inset depicts the measurement geometry. The XNLD difference (LH-LV) with light polarized along (100) (LV) and (01$\bar{1}$) (LH) from experiment and calculations for both poling states of PMN-PT is shown in (b) and (d), respectively.

with $x = 0.3$ doping [33], the OOP poled state is created by applying the constraints of epitaxial growth [deduced from the RSMs Figs. 5(e) and 5(f) in Sec. III B] to all surrounding atoms: −0.4% compressive strain along the (011) direction, +2.5% tensile strain along the (01$\bar{1}$) direction, and +1.05% tensile strain along the (100) direction. Here, for the (100) direction the maximum (1.5% tensile strain) extracted from the LSMO reflection in Fig. 5(f) was assumed to present an average of domains in the OOP poled (1.05% tensile strained) and the IP poled (1.95% tensile strained) configuration, keeping in mind the PMN-PT lattice parameter change of +0.9% upon switching. XNLD spectra are calculated for $LaMnO_3$ as well as for $SrMnO_3$ and weighted according to the doping concentration of LSMO $x = 0.3$. The XNLD of the latter is about four times smaller, because $Mn^{4+}$ with a half-filled $t_{2g}$ triplet and unoccupied $e_g$ orbitals is not a Jahn-Teller active ion. The resulting calculated XNLD difference spectrum obtained for the OOP poled case is shown in black in Fig. 6(d). To simulate LSMO in the IP poled state the procedure is the same, but the coordinate files are further strained applying the strain values upon switching deduced from the PMN-PT RSMs [Figs. 5(a)–5(d)], i.e., an additional tensile strain of +0.9% along (100), as well as compressive strains of −0.23% along (01$\bar{1}$) and −0.7% along (011). The calculated XNLD difference spectrum obtained for the IP poled case would represent a single IP poled domain. The RSMs in Sec. III B gave an IP/OOP domain distribution ∼ 60/40. To compare with the measured XNLD, the simulations obtained for IP poled state and OOP poled state were averaged accordingly. This averaged XNLD spectrum representing the IP poled state is shown in Fig. 6(d) in red. The multiplet calculations reproduce the experimental trends well as can be seen when comparing Figs. 6(b) and 6(d). This emphasizes that the crystal field change plays the key role to reproduce the spectroscopic features, since strain values representing epitaxial growth yield the correct line shape of the difference spectrum. Note that the first peak at 637 eV in the calculated difference spectrum is absent in the measured XNLD. This feature is also produced by other multiplet approaches, where the crystal field is introduced in a parameterized form depending on the point group in consideration [22,23]. Switching from an OOP state to an IP poled state, the intensity of the difference spectrum doubles due to the additional strain, but the line shape of the XNLD does not change in agreement with experiment.

The $LaMnO_3$ crystal lattice strained to represent either the geometry of an OOP or an IP poled state is used as an input for DFT band-structure (DMol$^3$) [42] calculations

in order to investigate the orbital occupation. The strain leads to a redistribution of the 3$d$ ground state population representing the $e_g$ orbitals. The OOP poled state yields an excess population ~2.1% of orbitals oriented parallel to the surface plane ($d_{x^2-y^2}$) over orbitals pointing perpendicular ($d_{z^2}$). In the IP poled state the population imbalance amongst the $e_g$ orbitals increases to 5.1%. As the experimental geometry probes the $d_{x^2-y^2}$ population along the in-plane (100) direction with LV polarized light, an intensity increase of the difference spectrum (LH-LV) upon IP poling corresponds to a smaller density of empty states along the (100) direction probed with vertical polarized light, i.e., an increase of the population parallel to the surface.

## IV. DISCUSSION

In this study, we observe a $T_C$ shift of 10 K due to electrical switching in both XMCD measurements along the $(01\bar{1})$ direction and resistance measurements. Hence, the switching does not simply induce a mere rotation of the easy axis as previously reported [24] but a real $T_C$ shift. A similar magnitude in $T_C$ change has been previously only observed in applied electric fields [21] or under hydrostatic compression [11] with a change of about 1.45 K/kbar. In contrast, our results show a reversible change in remanence, which can be understood along the lines of the model proposed by Millis and coworkers [9]. An anisotropic tensile strain changes Mn-O-Mn bond angles and increases the Mn-O distances, thus reducing the in-plane electron transfer. As a consequence the ferromagnetic double exchange mechanism is reduced leading to a general decrease in $T_C$. In the case of LSMO/PMN-PT (011) we observe a large tensile in-plane strain change upon switching ~0.9% along the (100) direction, which contains a Mn-O-Mn bond chain. We note that our measured relative PMN-PT lattice changes deviate from reported strain gauge measurements [27]. Some of the strain gauge measurements were done with thick Pt electrodes, that can lead to an underestimation of the strain changes [24,27]. Here, we are directly distorting the LSMO lattice adjacent to the PMN-PT surface.

In the IP poled state LSMO exhibits a smaller projected $m_{\mathrm{tot}}$ at remanence for all IP directions. The FM phase in LSMO below $T_C$ is characterized by the spontaneous alignment of Mn spins allowing for a delocalization of the $e_g$ electrons, as the double-exchange interaction is of FM character. The smaller projected spin moment and higher resistivity observed for the IP poled state corresponds to a reduced $e_g$ electron itinerancy and ultimately lower $T_C$ value. The fact that the saturation magnetization at 4 T remained the same for both strain states can be understood, recalling that a high magnetic field applied above $T_C$ can reinforce FM alignment of spins leading to an induced magnetism [8].

The strain changes upon switching lead to a different orbital occupation as seen in the XNLD spectra. When measured above $T_C$, they highlight changes in the crystal field upon switching. The multiX multiplet calculations for the IP and OOP poled state emphasize that the strain plays the key role to reproduce the spectroscopic features and is responsible for the crystal field change. They yield a good agreement between the experimental and calculated XNLD line shape and reproduce the XNLD intensity increase upon switching.

DFT calculations using the same strain states yield a redistribution of the $e_g$ population: For the OOP poled state, the occupation of orbitals oriented parallel to the surface plane is favored over the occupation of orbitals pointing perpendicular to the surface. For the IP poled state, this occupation imbalance is further enhanced. The DFT calculations support the picture that the energy difference between the $e_g$ levels is increased upon switching from OOP to IP, reinforcing the electron tendency to be localized, thus determining a reduction of the Curie temperature.

## V. CONCLUSION

In summary, this study demonstrated reversible electrical switching in LSMO/PMN-PT (011) resulting in a 10 K shift of the magnetic Curie temperature $T_C$. Two distinct remanent strain states can be set in the substrate by poling the FE polarization out-of-plane or parallel to the surface. The change in crystal field upon switching was probed by XNLD. MultiX multiplet calculations show that the change in Mn-O bond length due to the strain is of key importance to reproduce the XNLD spectral shape. DFT calculations support the picture that the structural modifications lead to a change in the population of the $e_g$ orbitals favoring orbitals that lie in the surface plane hence localizing the electrons. Both effects, the lowering of the $e_g$ itinerancy and the increase in the electron-lattice coupling, explain the reduction in $T_C$ in agreement with the Millis model.

## ACKNOWLEDGMENTS

The x-ray absorption measurements were performed on the EPFL/PSI X-Treme beamline at the Swiss Light Source, Paul Scherrer Institut, Villigen, Switzerland. The manganite film was grown at the Takamura laboratory in the Department of Chemical Engineering and Materials Science, University of California, Davis. We thank Christof Schneider for his assistance in structural characterization and Marcus Schmidt for technical support. This work was supported by the Swiss Nanoscience Institute, University of Basel, the Swiss National Science Foundation (SNF) projects 206021-139102 and 200020-153660, as well as the EU's 7th Framework Program IFOX (NMP3-LA-2010 246102).

[1] C. A. F. Vaz, J. Phys.: Condens. Matter **24**, 333201 (2012).

[2] D. Pantel, S. Goetze, D. Hesse, and M. Alexe, Nat. Mater. **11**, 289 (2012).

[3] Y. Wang, J. Hu, Y. Lin, and C.-W. Nan, NPG Asia Mater **2**, 61 (2010).

[4] M. Y. Zhuravlev, S. Maekawa, and E. Y. Tsymbal, Phys. Rev. B **81**, 104419 (2010).

[5] J. Rondinelli, M. Stengel, and N. Spaldin, Nat. Nano. **3**, 46 (2008).

[6] H. J. A. Molegraaf, J. Hoffman, C. A. F. Vaz, S. Gariglio, D. van der Marel, C. H. Ahn, and J.-M. Triscone, Advanced Materials **21**, 3470 (2009).

[7] O. Chmaissem, B. Dabrowski, S. Kolesnik, J. Mais, J. D. Jorgensen, and S. Short, Phys. Rev. B **67**, 094431 (2003).

[8] A.-M. Haghiri-Gosnet and J.-P. Renard, J. Phys. D: Appl. Phys. **36**, R127 (2003).

[9] A. J. Millis, T. Darling, and A. Migliori, J. Appl. Phys. **83**, 1588 (1998).

[10] Y. Moritomo, A. Asamitsu, and Y. Tokura, Phys. Rev. B **51**, 16491 (1995).

[11] V. Moshnyaga, S. Klimm, E. Gommert, R. Tidecks, S. Horn, and K. Samwer, J. Appl. Phys. **88**, 5305 (2000).

[12] F. Tsui, M. C. Smoak, T. K. Nath, and C. B. Eom, Appl. Phys. Lett. **76**, 2421 (2000).

[13] A. Tebano, C. Aruta, P. G. Medaglia, F. Tozzi, G. Balestrino, A. A. Sidorenko, G. Allodi, R. De Renzi, G. Ghiringhelli, C. Dallera, L. Braicovich, and N. B. Brookes, Phys. Rev. B **74**, 245116 (2006).

[14] C. Adamo, X. Ke, H. Q. Wang, H. L. Xin, T. Heeg, M. E. Hawley, W. Zander, J. Schubert, P. Schiffer, D. A. Muller, L. Maritato, and D. G. Schlom, Appl. Phys. Lett. **95**, 112504 (2009).

[15] H. Boschker, J. Kautz, E. P. Houwman, W. Siemons, D. H. A. Blank, M. Huijben, G. Koster, A. Vailionis, and G. Rijnders, Phys. Rev. Lett. **109**, 157207 (2012).

[16] J. Fontcuberta, V. Laukhin, and X. Obradors, Appl. Phys. Lett. **72**, 2607 (1998).

[17] H. Y. Hwang, S.-W. Cheong, P. G. Radaelli, M. Marezio, and B. Batlogg, Phys. Rev. Lett. **75**, 914 (1995).

[18] H. Y. Hwang, T. T. M. Palstra, S.-W. Cheong, and B. Batlogg, Phys. Rev. B **52**, 15046 (1995).

[19] J. Fontcuberta, B. Martinez, A. Seffar, S. Piñol, J. L. Garćia-Muñoz, and X. Obradors, Phys. Rev. Lett. **76**, 1122 (1996).

[20] Y. Suzuki, H. Y. Hwang, S.-W. Cheong, and R. B. van Dover, Appl. Phys. Lett. **71**, 140 (1997).

[21] C. Thiele, K. Dörr, O. Bilani, J. Rödel, and L. Schultz, Phys. Rev. B **75**, 054408 (2007).

[22] A. Tebano, C. Aruta, S. Sanna, P. G. Medaglia, G. Balestrino, A. A. Sidorenko, R. De Renzi, G. Ghiringhelli, L. Braicovich, V. Bisogni, and N. B. Brookes, Phys. Rev. Lett. **100**, 137401 (2008).

[23] D. Pesquera, G. Herranz, A. Barla, E. Pellegrin, F. Bondino, E. Magnano, F. Sánchez, and J. Fontcuberta, Nat. Commun. **3**, 1189 (2012).

[24] Y. Yang, M. Meng Yang, Z. L. Luo, H. Huang, H. Wang, J. Bao, C. Hu, G. Pan, Y. Yao, Y. Liu, X. G. Li, S. Zhang, Y. G. Zhao, and C. Gao, Appl. Phys. Lett. **100**, 043506 (2012).

[25] A. Bokov and Z.-G. Ye, J. Mater. Sci. **41**, 31 (2006).

[26] B. Noheda, D. E. Cox, G. Shirane, J. Gao, and Z.-G. Ye, Phys. Rev. B **66**, 054104 (2002).

[27] T. Wu, P. Zhao, M. Bao, A. Bur, J. L. Hockel, K. Wong, K. P. Mohanchandra, C. S. Lynch, and G. P. Carman, J. Appl. Phys. **109**, 124101 (2011).

[28] J. Stoehr and H. Siegmann, *Magnetism: From Fundamentals to Nanoscale Dynamics*, Springer Series in Solid-State Sciences (Springer, Berlin, Heidelberg, New York, 2006).

[29] C. Piamonteze, U. Flechsig, S. Rusponi, J. Dreiser, J. Heidler, M. Schmidt, R. Wetter, M. Calvi, T. Schmidt, H. Pruchova, J. Krempasky, C. Quitmann, H. Brune, and F. Nolting, Journal of Synchrotron Radiation **19**, 661 (2012).

[30] P. Carra, B. T. Thole, M. Altarelli, and X. Wang, Phys. Rev. Lett. **70**, 694 (1993).

[31] C. T. Chen, Y. U. Idzerda, H.-J. Lin, N. V. Smith, G. Meigs, E. Chaban, G. H. Ho, E. Pellegrin, and F. Sette, Phys. Rev. Lett. **75**, 152 (1995).

[32] A. Uldry, F. Vernay, and B. Delley, Phys. Rev. B **85**, 125133 (2012).

[33] Inorganic Crystal Structure Database, http://icsd.fiz-karlsruhe.de/icsd, ICSD Collection Code 186700.

[34] T. Saitoh, A. E. Bocquet, T. Mizokawa, H. Namatame, A. Fujimori, M. Abbate, Y. Takeda, and M. Takano, Phys. Rev. B **51**, 13942 (1995).

[35] T. Koide, H. Miyauchi, J. Okamoto, T. Shidara, T. Sekine, T. Saitoh, A. Fujimori, H. Fukutani, M. Takano, and Y. Takeda, Phys. Rev. Lett. **87**, 246404 (2001).

[36] R. D. Cowan, *The Theory of Atomic Structure and Spectra*, Los Alamos Series in Basic and Applied Sciences (University of California Press, Berkeley, CA, 1981).

[37] C. Zener, Phys. Rev. **82**, 403 (1951).

[38] A. Anane, C. Dupas, K. L. Dang, J. P. Renard, P. Veillet, A. M. de Leon Guevara, F. Millot, L. Pinsard, and A. Revcolevschi, J. Phys. Condens. Matter **7**, 7015 (1995).

[39] G. Jonker and J. V. Santen, Physica **16**, 337 (1950).

[40] A. Urushibara, Y. Moritomo, T. Arima, A. Asamitsu, G. Kido, and Y. Tokura, Phys. Rev. B **51**, 14103 (1995).

[41] R. V. Chopdekar, E. Arenholz, and Y. Suzuki, Phys. Rev. B **79**, 104417 (2009).

[42] B. Delley, J. Chem. Phys. **92**, 508 (1990).